Glia

WILEY

GLIA

RESEARCH ARTICLE OPEN ACCESS

The X-Linked Intellectual Disability Gene, *ZDHHC9*, Is Important for Oligodendrocyte Subtype Determination and Myelination

Rocio B. White[1] | Angela R. Wild[1] | Timothy P. O'Leary[1] | Andrew J. Thompson[1] | Stephane Flibotte[2] | Angie Peng[1] | Jason C. Rogalski[3] | Mila Mair[1] | Neeki Derhami[1] | Shernaz X. Bamji[1]

[1]Department of Cellular and Physiological Sciences, Life Sciences Institute and Djavad Mowafaghian Centre for Brain Health, University of British Columbia, Vancouver, British Columbia, Canada | [2]Life Sciences Institute Bioinformatics Facility, University of British Columbia, Vancouver, British Columbia, Canada | [3]Department of Biochemistry and Molecular Biology, University of British Columbia, Vancouver, British Columbia, Canada

Correspondence: Shernaz X. Bamji (shernaz.bamji@ubc.ca)

Received: 24 June 2024 | **Revised:** 4 March 2025 | **Accepted:** 6 March 2025

Funding: This work was supported by Canadian Institutes of Health Research, F18-00650.

Keywords: corpus callosum | myelination | oligodendrocytes | palmitoylation | X-linked intellectual disability

ABSTRACT

Two percent of patients with X-linked intellectual disability (XLID) exhibit loss-of-function mutations in the enzyme, ZDHHC9. One of the main anatomical deficits observed in these patients is a decrease in corpus callosum volume and a concurrent disruption in white matter integrity. In this study, we demonstrate that deletion of *Zdhhc9* in mice disrupts the balance of mature oligodendrocyte subtypes within the corpus callosum. While overall mature oligodendrocyte numbers are unchanged, there is a marked increase in MOL5/6 cells that are enriched in genes associated with cell adhesion and synapses, and a concomitant decrease in MOL2/3 cells that are enriched in genes associated with myelination. In line with this, we observed a decrease in the density of myelinated axons and disruptions in myelin compaction in the corpus callosum of *Zdhhc9* knockout mice. RNA sequencing and proteomic analysis further revealed a reduction in genes and proteins essential for lipid metabolism, cholesterol synthesis, gene expression, and myelin compaction, offering insights into the underlying mechanisms of the pathology. These findings reveal a previously underappreciated and fundamental role for ZDHHC9 and protein palmitoylation in regulating oligodendrocyte subtype determination and myelinogenesis, offering mechanistic insights into the deficits observed in white matter volume in patients with mutations in *ZDHHC9*.

1 | Introduction

ZDHHC9 is one of a family of 23 palmitoyl acyl transferases that catalyze *S*-acylation, the reversible addition of acyl groups onto proteins through a labile thioester bond (Chamberlain and Shipston). In the brain, palmitoylation is the most common form of *S*-acylation and directly influences protein trafficking, function, and stability (Chamberlain and Shipston 2015). Loss-of-function (LOF) mutations in the *ZDHHC9* gene (which is located on the X-chromosome) have been reported in ~2% of male patients diagnosed with X-linked intellectual disability (XLID) (Raymond et al. 2007; Tzschach et al. 2015; Masurel-Paulet et al. 2014; Schirwani et al. 2018; Boone et al. 2010; Han et al. 2017, 2018; Grozeva et al. 2015), with ~75% of these patients exhibiting epileptic comorbidities (Baker et al. 2015). Deletion of *Zdhhc9* in mice (Gene nomenclature: "*ZDHHC9*" in humans and "*Zdhhc9*" in mice) results in cognitive deficits that mirror those observed in human patients (Kouskou et al. 2018). We have

Angela R. Wild, Timothy P. O'Leary are authors who contributed equally.

shown that ablating *Zdhhc9* can profoundly reduce dendritic branching, disrupt the formation of inhibitory synapses, and increase seizure-like activity (Shimell et al. 2019).

Magnetic Resonance Imaging (MRI) on patients (Masurel-Paulet et al. 2014; Schirwani et al. 2018; Boone et al. 2010; Baker et al. 2015) and mice (Kouskou et al. 2018) lacking ZDHHC9 demonstrates a striking decrease in the volume of the corpus callosum, a large white matter tract that connects the two hemispheres of the brain (Bathelt et al. 2016). In accordance with this, single-cell (scRNAseq) studies reveal that *Zdhhc9* is most highly expressed in the corpus callosum and in myelinating oligodendrocytes (Wild et al. 2022). Notably, *Zdhhc9* is the most highly expressed palmitoylating enzyme in oligodendrocytes at postnatal day 23 (Marques et al. 2016)—the period of peak myelination of the corpus callosum (Sturrock 1980). Even though ZDHHC9 is highly expressed in the corpus callosum and that the volume of the corpus callosum is significantly attenuated in patients and mice lacking ZDHHC9, the role of ZDHHC9 in white matter development remains unexplored.

White matter development is dependent on the proper differentiation of oligodendrocytes, which comprise > 70% of cells in the corpus callosum (Codeluppi et al. 2018). Oligodendrocyte differentiation is a stepwise process that starts with oligodendrocyte precursor cells (OPCs) that differentiate into newly formed oligodendrocytes (NFOLs), then myelin-forming oligodendrocytes (MFOLs), and finally mature oligodendrocytes (MOLs) (Marques et al. 2016). Recent scRNAseq studies have demonstrated further transcriptomic heterogeneity within the four main oligodendrocyte groups, including 2 NFOL subtypes (NFOL1,2), 2 MFOL subtypes (MFOL1,2) and 6 MOL subtypes (MOL1-6) (Marques et al. 2016; Hilscher et al. 2022) that can be distinguished by unique gene expression signatures. For example, MOL2/3 cells are enriched in myelin-related and cholesterol biosynthesis genes, while MOL5/6 cells exhibit high expression of synapse and cell–cell adhesion genes (Marques et al. 2016).

Here, we show that although the ablation of ZDHHC9 does not impact the overall number of oligodendrocyte lineage cells, it is required for the proper determination of MOL subtype proportions in the corpus callosum, with *Zdhhc9*-knockout (KO) mice exhibiting a decrease in MOL2/3 subtype cells and a concomitant increase in MOL5/6 cells. The decrease in MOL2/3 cells that are transcriptionally enriched for genes associated with myelination was accompanied by a decrease in the number of myelinated axons and disruptions in myelin compaction and integrity in the corpus callosum of KO mice. In addition, we observed reduced expression of genes and proteins essential for lipid metabolism, cholesterol synthesis, and myelin compaction. Together, this study provides a mechanistic understanding of the role of ZDHHC9 in white matter and how LOF mutations in Zdhhc9 lead to reduced callosal size and interhemispheric communication deficits in XLID.

2 | Materials and Methods

2.1 | Mice

Zdhhc9-KO mice (B6;129S5-Zdhhc9tm1Lex/Mmucd) were originally obtained from the Mutant Mouse Resource and Research Center (MMRRC, University of California Davis). A mutation in *Zdhhc9* was introduced through homologous recombination, targeting coding exon 1 (NCBI ascension: NM_172465.1). All experiments were performed on mice between 2 and 4 months of age, except for analysis of the myelin proteome, where mice were 23 days of age. Mice were housed in same-sex groups of 2–5 within optimouse cages, with bedding, a plastic hut, and nesting material for enrichment. Food and water were available *ad libitum*. Ear notches were collected at weaning (21 days of age) for identification, and genotyped by Transnetyx (Cordova, TN). All procedures followed guidelines from the Canadian Council on Animal Care and were approved by the UBC Animal Care Committee.

2.2 | Fluoromyelin Staining and Analysis

Thickness and area measurements were obtained across six regions (each 350-600um in length) spanning the anterior–posterior axis of the corpus callosum. Measurements were obtained from within each of the Genu (1.1 to 0.26), Body (−0.01 to −1.34) and Splenium (−1.45 to −2.54) of the corpus callosum, based on stereotaxic coordinates in Franklin and Paxinos (Franklin and Paxinos 2008). For each mouse, 2–5 sections were sampled from each region, and measures were obtained either at midline or averaged bilaterally across cerebral hemispheres.

2.3 | Tissue Collection for RNA-Sequencing

Mice were anesthetized under isoflurane (5%, 1.5 L/min) and decapitated. Brains and optic nerves were dissected and flash frozen in pre-chilled isopentane at −52°C for 30 s. Brains were then stored at −80°C until sectioning. The corpus callosum (Bregma 0.98 mm—Bregma 0.62 mm) was sectioned coronally at 100 μm on a cryostat and mounted onto glass slides. Slides were then stored at −80°C until used. Corpus callosum samples were dissected from frozen brain sections while being cooled on dry ice. RNA was extracted from samples using the Total RNA Purification Micro Kit (Cat. 35,300, Norgen Biotek Corp) following the supplied protocol. Samples were then kept at −80°C until analyzed by the RNA sequencing core at the School of Biomedical Engineering Sequencing Core at the Biomedical Research Center (University of British Columbia).

2.4 | RNA-Sequencing

Sample quality control was performed using the Agilent 2100 Bioanalyzer or the Agilent 4200 Tapestation. Qualifying samples were then prepped following the standard protocol for the Illumina Stranded mRNA prep (Illumina). Sequencing was performed on the Illumina NextSeq2000 with Paired End 59 bp × 59 bp reads.

2.5 | RNA-Sequencing Analysis

RNA-seq raw sequencing reads were processed with kallisto (Bray et al. 2016) using the reference transcriptome for mm10 downloaded from Ensembl (www.ensembl.org) and the resulting counts for different isoforms were summed up to obtain

counts at the gene level for each sample. The differential expression analysis was then performed with DESeq2 (Love et al. 2014) and genes achieving the significance cut-off of FDR < 0.05 were considered significantly differentially expressed. Marker genes for each cell type were extracted from the file l5_all.agg.loom downloaded from the Mousebrain website (http://mousebrain.org/adolescent/downloads.html).

2.6 | Quantitative PCR

Total RNA was extracted from samples using the Total RNA Purification Micro Kit (Cat. 35,300, Norgen Biotek Corp) following the supplied protocol. Quantitative PCR with reverse transcription was performed on a ViiA 7 instrument (Thermo Fisher Scientific) using SYBR Green master mix (Thermo Fisher Scientific). The relative amounts of the messenger RNAs studied were determined by means of the $2^{-\Delta\Delta T}$ method, with Gapdh as the reference gene and the control genotype as the invariant control.

2.7 | Bioinformatics

Biological process enrichment analysis was done using the PANTHER overrepresentation test (Released 2022-10-13). Functional interaction networks of the differentially expressed genes were investigated using the Search Tool for the Retrieval of Interacting Genes (STRING) 11.5 (Szklarczyk et al. 2019). A threshold confidence level of 0.4 was used to identify protein interactions, and seven types of protein interactions were used for network generation, including neighborhood, gene fusion, co-occurrence, co-expression, experimental, database knowledge, and text mining. The Mouse Genome Informatics (RRID:SCR_006460) database (Baldarelli et al. 2021) was used to assign GO classifications for the list of differentially expressed genes and differentially expressed proteins. Cell type proportion estimates were performed using Bisque deconvolution (Kvilekval et al. 2010) of our RNAseq data using the Brain Initiative Cell Census Network 2.0 (Yao et al. 2023) as the reference scRNAseq dataset. Clusters from Yao et al. (2023) were mapped onto the widely adopted nomenclature (Marques et al. 2016; Hilscher et al. 2022; Floriddia et al. 2020; Wang et al. 2023; Pandey et al. 2022) used for oligodendrocyte lineage first defined by Marques et al. (2016) using the expression of marker genes in each cluster: clusters 5266–5271 = OPC, 5272–5277 = COP, 5280 = NFOL1, 5281 = NFOL2, 5283 = MFOL1, 5282 = MFOL2, 5288 = MOL1, 5284 & 5286 = MOL2/3, 5285 and 5287 = MOL5/6.

2.8 | Fluorescent In Situ Hybridization

Fluorescent in situ hybridization was performed with target retrieval, pretreatment, hybridization, amplification, and detection according to the RNAscope Multiplex Fluorescent Reagent Kit v2 Assay User Manual for Fixed Frozen Tissue (ACD). Multiplexed FISH probes for *Pdgfra* (480661-C2), *Itpr2* (579391-C3), *Ctps* (1149611-C4), *Wfdc18* (430051-C2), *Hapln2* (1149621-C1), *Ptgds* (492781-C4), and *C030029H02Rik* (1301981-C3) were used as marker gene probes to identify OPCs, NFOLs, MFOLs, MFOL2, MOL2/3, and MOL5/6, respectively. *Wfdc18* was used as a marker to verify cells were not MFOLs. Slides were cover slipped with Prolong Gold Antifade Mountant (Invitrogen, Cat. P36930). Once dried, slides were kept at 4°C until imaged.

2.9 | Fluorescent In Situ Hybridization Analysis

First, a region of interest was created around the corpus callosum using the polygon tool in FIJI. Cell ROIs within the corpus callosum were then generated from the DAPI channel using a custom FIJI macro. In short, the macro consisted of auto thresholding the image, converting the image to a mask, applying Gaussian blur (sigma = 3), binarizing the image, inverting the image, applying Watershed, and dilating particles by 1 μm. Finally, only nuclei between 50 and 310 μm^2 and a circularity of 0.5–1.0 were selected for analysis. *Pdgrfa*, *Itpr2*, and *Ctps* channels were then each individually thresholded, and percent coverage for each probe was measured in each cell ROI. Cells were assigned as OPC, NFOL, or MFOL according to the marker probe with the highest percent coverage in each cell nucleus. Cells were only counted that had a dominant probe percentage coverage > 4% (minimum marker gene expression).

For MOL2/3 and MOL5/6 analysis, a similar region of interest was created around the corpus callosum in FIJI. Nuclei were then identified and segmented from the maximum intensity projection image using the Identify Primary Objects module in Cell Profiler v4.2.6 (Carpenter et al. 2006). Nuclei were then dilated by 3 pixels to capture near-nuclear RNAscope staining. A label image of the segmented nuclei was identified and used to make nuclear ROIs in FIJI through the "Label Image to ROIs" plugin from the PTBIOP update site. RNAscope channels were manually thesholded as above and percent coverage per cell measured. Cell assignment was carried out in R v4.3.2 using RStudio v2023.12.1.402 (Posit Software) as described previously (Floriddia et al. 2020). Briefly, cells were assigned to MOL2/3 if their *Hapln2* coverage exceeded an empirical threshold (16%) of the nuclear area and if their *Hapln2* coverage was greater than the *Hapln2* area was greater than the *Ptgds* position. Cells were assigned to MOL5/6 if their *Ptgds* coverage was greater than 7% of nuclear area. As *Ptgds* alone does not mark MOL5/6 exclusively (Figure S4a), we additionally filtered this class of cells for inclusion of the long non-coding RNA *C030029H02Rik* and exclusion of the MFOL2 marker *Wfdc18*.

2.10 | Immunostaining

All immunostaining was completed on free-floating sections. Sections were first washed in PBS (0.1 M, pH 7.4), 3 times for 5 min. Antigen retrieval was then completed by incubating sections in a sodium citrate buffer (10 mM, pH 6.0) with Tween 20 (0.5%) for 20 min at 80°C. Sections were then cooled and were incubated in PBS with 0.1% triton-X (PBS-TX) and 10% goat serum for 3 h to reduce subsequent non-specific antibody binding. The sections were then incubated in PBS-TX with 5% goat serum containing primary antibodies for $Na_v1.6$ (1:500 dilution, ASC-009, Alomone); or Olig2 (1:500, NBP1-28667, Novus) and CC-1 (1:100, ab16794, Abcam); or GFAP (1:500, ab7260, Abcam) and Iba1 (1:500, ab178846, Abcam); or Olig2

(1:500, NBP1-28667, Novus) and Ki67 (1:500, ab15580, Abcam); or Olig2 (1:500, NBP1-28667, Novus) and CC3 (1:500, 9661S, Cell Signaling Techno) were incubated overnight at 4°C. Following primary antibody incubation, sections were washed in PBS-TX (3 × 5 min) and incubated in PBS-TX containing secondary goat anti-rabbit AlexaFluor 488 (1:500 dilution, Ab150077, Abcam) or goat anti-mouse AlexaFluor 488 (1:500, A-21141, Invitrogen) and goat anti-rabbit AlexaFluor 647 (1:500, A-21244, Invitrogen). Sections were then washed in PBS-TX (3 × 5 min) and counterstained with DAPI (1:500) in PBS-TX for 10 min. Lastly, sections were washed in PBS (3 × 5 min), mounted onto Superfrost Plus glass slides (Fisher Scientific), and coverslips were applied using the ProLong Gold anti-fade (Invitrogen) mounting medium.

2.11 | Electron Microscopy Sample Preparation

Brains were first sectioned coronally on a vibratome (Leica, VT1000) at 200 μm thickness. Comparable posterior sections (−1.82 to −2.30 from Bregma) were selected for each animal, and sections were washed three times in sodium cacodylate buffer (0.1 M). The hemispheres of each section were bisected using a razor blade, and a brain punch (0.50 mm, Ted Pella) was used to make a fiducial hole dorsal to the corpus callosum. Samples were then post-fixed with 1% osmium tetroxide and 1.5% potassium ferricyanide, stained *en bloc* with 2% uranyl acetate, dehydrated in an alcohol series, and finally embedded in Epon 812 resin (Electron Microscopy Sciences). 70 nm ultra-thin sagittal sections were obtained along the medial edge of the corpus callosum using an ultramicrotome (UC7, Leica) and mounted onto 2 × 1 mm Formvar-coated copper slots (Electron Microscopy Sciences). Ultra-thin sections were then grid-stained with 2% uranyl acetate for 12 min and Reynolds' lead citrate stain for 6 min. Slots were imaged on a FEI Tecnai Spirit transmission electron microscope at 80 kV. Images of the corpus callosum were taken in the dorsal region of the corpus callosum.

2.12 | Electron Microscopy Analysis

For each animal, 1–4 images taken in the dorsal region of the corpus callosum within 100 μm of the top of the corpus callosum at 9300× magnification (105.3 μm^2), ~100–300 axons per image, were analyzed using software for semi-automatic myelin *g*-ratio quantification (Myeltracer (Kaiser et al. 2021)). Myelinated axons with myelin loops and splitting of myelin were classified as axons with myelin abnormalities. To assess myelin decompaction, 10–15 higher magnification images were taken at 68,000× magnification, and ~20 axons per animal were analyzed.

2.13 | Microscopy

All myelin markers, nodal markers, and fluorescent in situ hybridization images were obtained using a Zeiss LSM 880 confocal microscope equipped with 405, 488, 543, 594, and 633 laser lines, three multialkali spectral PMTs, and an Airyscan detector. Images of fluoromyelin were obtained at a single optical plane using a 20×/0.8 NA objective with tile scans. Images of fluorescent in situ hybridization were acquired with a 63×/1.4 NA oil objective and were comprised of *Z*-stacks taken at 1.00 μm intervals through the entire section. Immunohistochemistry images were acquired using the Airyscan detector in the FastAiry mode. Tile scans covering the medial corpus callosum were acquired, maximum intensity *Z*-projected, and stitched in Zen Black software (Zeiss). All images were obtained using optimized laser settings for all five channels that were identical between sections.

2.14 | Myelin Purification

A myelin-enriched membrane fraction was biochemically purified from mouse brains by sucrose density centrifugation and osmotic shocks as described previously (Erwig et al. 2019; Jahn et al. 2020). Briefly, flash-frozen mouse brains were thawed in 0.32 M sucrose supplemented with protease inhibitor cocktail tablets (cOmplete Mini EDTA-free; Roche, Mannheim, Germany). Thawed brains were next manually homogenized using a pestle and 16G/25G needle. Brain homogenate was then layered carefully on top of 0.85 M sucrose and centrifuged. Following the first sucrose gradient, the band of the myelin-enriched fraction found at the 0.32 M/0.85 M sucrose interphase was collected and washed with distilled water. Two osmotic shocks using cold water were used to diminish cytoplasm and microsomes, followed by a second sucrose gradient and washing. To delipidate the purified myelin, protein samples underwent a series of methanol, chloroform, and distilled water washes.

2.15 | Liquid-Chromatography-Tandem Mass-Spectrometry (LC–MS/MS)

Myelin protein samples, boiled in SDS sample buffer, were run on a 10% SDS/PAGE gel. Proteins were detected with colloidal Coomassie G-250 and digested out of the gel as described previously (Chan et al. 2006). Samples were purified by solid phase extraction on C-18 STop And Go Extraction (STAGE) Tips. Samples were separated using a NanoElute UHPLC system (Bruker Daltonics) with an Aurora Series Gen2 (CSI) analytical column (25 cm × 75 μm 1.6 μm FSC C18, with Gen2 nanoZero and CSI fitting; Ion Opticks, Parkville, Victoria, Australia) heated to 50°C (by Column toaster M, Bruker Daltonics) and coupled to timsTOF Pro (Bruker Daltonics) operated in DDA-PASEF mode. In a standard 60 min run, the gradient was from 2% B to 12% B over 30 min, then to 33% B from 30 to 60 min, then to 95% B over 0.5 min, held at 95% B for 7.72 min. Before each run, the analytical column was conditioned with 4 column volumes of buffer A, where buffer A consisted of 0.1% aqueous formic acid and 0.5% acetonitrile in water, and buffer B consisted of 0.1% formic acid in 99.4% acetonitrile. The NanoElute thermostat temperature was set at 7°C. The analysis was performed at a 0.3 μL/min flow rate.

The Trapped Ion Mobility—Time of Flight Mass Spectrometer (TimsTOF Pro; Bruker Daltonics, Germany) was set to Parallel Accumulation-Serial Fragmentation (PASEF) scan mode for DDA acquisition scanning 100–1700 m/z with 5 PASEF ramps. The capillary voltage was set to 1800 V, drying gas to 3 L/min, and drying temperature to 180°C. The MS and MS/MS spectra were acquired from m/z 100 to 1700. As for the TIMS setting, the ion mobility range (1/k0) was set to

0.70–1.35 V·s/cm^2, 100 ms ramp time and accumulation time (100% duty cycle), and a ramp rate of 9.42 Hz; this resulted in 0.64 s of total cycle time.

Linear precursor repetitions were applied with a target intensity of 21,000 and a 2500 intensity threshold. The active exclusion was enabled with a 0.4 min release. The collision energy was ramped linearly as a function of mobility from 27 eV at 1/k0 = 0.7 V·s/cm^2 to 55 eV at 1/k0 = 1.35 V·s/cm^2. Isolation widths were set at 2.07 m/z at < 400 m/z and 3.46 m/z at > 1000 m/z.

Mass accuracy: the error of mass measurement is typically within 3 ppm and is not allowed to exceed 7 ppm. For the calibration of the ion mobility dimension, the ions of Agilent ESI-Low Tuning Mix were selected (m/z [Th], 1/k0 [Th]: 622.0290, 0.9915; 922.0098, 1.1986; 1221.9906, 1.3934).

TimsTOF Pro was run with timsControl v. 3.0.0 (Bruker). LC and MS were controlled with HyStar 6.0 (6.0.30.0, Bruker).

2.16 | Protein Search and Analysis

Data was analyzed with Fragpipe V18.0, MSFragger V3.5, Philosopher V4.4.0 (Kong et al. 2017) and quantitation performed using the MaxLFQ algorithm with match between runs enabled (Collins et al. 2017; Meier et al. 2018). The searches were matched to a *mus musculus* database downloaded from uniprot.org (reviewed sequences; RRID:SCR_002380) and a contaminant and decoy database. Default search parameters were used except for the following: 50 ppm mass tolerances were used for each of the MS and MS/MS, and MSMS was not required for LFQ. Accurately identified peptides were only confined to those with IonScores higher than 99% confidence. Contaminant and reverse hits were removed.

In LFQ, the intensities of the thus recorded peaks are taken as proxies for peptide abundance, with fragmentation spectra (MS2 spectra) used for peptide identification. In LFQ, each sample was separately analyzed on the mass spectrometer, and differential expression was obtained by comparing relative intensities between runs for the same identified peptide (Goeminne et al. 2018). Log ratios were calculated as the difference in average $\log_2$ LFQ intensity values between control and *Zdhhc9*-KO groups.

2.17 | Western Blot Analysis

Myelin from four control and four *Zdhhc9*-KO P23 mice was extracted as previously described in 2.14. Following lipid removal, myelin proteins were resuspended in RIPA lysis buffer. Protein concentration was measured using a Pierce BCA Protein Assay kit (23,225; Thermo Scientific) and samples were diluted to a concentration of 3 μg/μL. 30 μg of protein was loaded onto 10% or 12% Tris-Glycine resolving gels with a 4% stacking gel and wet transferred onto a PVDF membrane for 1 h at 4°C. Blots were blocked for 1 h with BSA (ALB001; Bioshop) before incubation with primary antibodies overnight at room temperature (MAG: 1:1000 dilution, 34–62,000, Invitrogen; MBP: 1:1000 dilution, NB600-717, Novus bio; MOBP: 1:1000 dilution, #PA5-100618, Invitrogen; CLDN11: 1:1000, 36–4500, Invitrogen; MOG: 1:1000 dilution, ab233549, Abcam; SIRT2: 1:2000 dilution, ab211038, Abcam; GAPDH: 1:1000 dilution, MA5-15738, Invitrogen). Blots were incubated with HRP-conjugated secondary antibodies (goat anti-rabbit IgG (H + L): 1:3000 dilution, 65–6120, Invitrogen; goat anti-rat IgG: 1:3000 dilution, ab97057, Abcam; goat anti-mouse IgG (H + L): 1:3000 dilution, 62–6520, Invitrogen) for 1 h at room temperature. Blots were incubated with Immubilon Crescendo Western HRP substrate (WBLUR0100; Millipore Sigma) for 1 min immediately prior to imaging on a BioRad Chemi-Doc MP (serial number: 731BR02628). Western blot protein level quantification was done on Fiji using the gel analysis tools. Protein levels were normalized to each lane's respective loading control (GAPDH) signal. Finally, protein levels were normalized to the average control expression for each respective protein tested.

2.18 | Statistical Analyses

Prior to analysis, normality and homogeneity of variance were tested for. All values in graphs report the mean ± standard error of the mean. Fluoromyelin staining, FISH, TEM, nodal staining, and proteomics data was analyzed with unpaired two-tailed Student's *t*-tests ($p < 0.05$). TEM axon size and g-ratio distribution analyses were completed using the Kolmogorov–Smirnov test. All major statistical analyses, outlier analyses, and graph generation were conducted using GraphPad Prism (Version 8.4.3) software (GraphPad, CA, United States). Asterisks and hashtags are used to denote levels of statistical significance within all graphs (*$p < 0.05$; **$p < 0.01$; ***$p < 0.001$).

3 | Results

3.1 | Uniform Reduction in Corpus Callosum Width Throughout the Anterior–Posterior Axis in *Zdhhc9*-KO Mice

Axonal organization in the corpus callosum is heterogeneous and organized in a spatially segregated manner according to projection neuron origin and corresponding targets in the contralateral hemisphere (Ku and Torii 2020) (Figure S1a). Despite this heterogeneity, we observed a robust and relatively homogeneous reduction in the width of the corpus callosum, hippocampal commissure, and external capsule in postnatal day 60 (P60) *Zdhhc9*-KO male mice at all regions analyzed along the antero-posterior axis (Figure S1a–f), as well as a relatively homogeneous expression of *Zdhhc9* along the anterior–posterior axis (Figure S1g,h). To date, only male patients have been identified to have XLID with *ZDHHC9* loss of function mutations (Raymond et al. 2007; Bathelt et al. 2016; Mir et al. 2023), and accordingly, only male mice were used in this study.

3.2 | Altered Corpus Callosum Gene Expression in *Zdhhc9*-KO Mice

To investigate whether there are any molecular alterations associated with changes in callosal volume, we performed bulk

RNAseq on the microdissected corpus callosum of control and *Zdhhc9*-KO mice (Figure 1a). We identified 173 differentially expressed genes (Dataset S1 for RNAseq raw data; Dataset S2 for the list of 173 differentially expressed genes organized by gene ontology {GO annotation}). Of the differentially expressed genes, 52 were upregulated and 121 genes were downregulated in *Zdhhc9*-KO mice (Figure 1b). Examination of the top upregulated and downregulated genes revealed frequent links to roles in oligodendrocyte development and function. Among the top downregulated genes (*Slco3a1, Apln, Slc45a3*, and *Cyp51*), both *Slc45a3* and *Cyp51* are known to play roles in lipid metabolism (Shin et al. 2012; Allimuthu et al. 2019), with other genes related to this process, such as *Ldlr, Hmgcs1, Insig1, Sqle*, and *Msmo1*, also showing reduced expression. Additionally, *Apln* has also been reported to enhance oligodendrocyte differentiation (Ito et al. 2021). The top five upregulated genes included *Svep1*, *Kit*, *Syt2*, *Fbxw15*, and *Oprk1*. Interestingly, both *Kit* and *Oprk1* have been associated with promoting oligodendrocyte proliferation (Hu et al. 2004; Mei et al. 2016; Du et al. 2016). Apart from *Zdhhc9* itself, no significant changes were observed in the expression levels of other ZDHHC enzymes or palmitoyl thioesterases (enzymes that catalyze the removal of palmitate), suggesting no compensatory changes in other enzymes that regulate palmitoylation at the transcriptional level (Dataset S1). Notably, of all the ZDHHC enzymes, *Zdhhc9* was the most highly expressed ZDHHC enzyme in the corpus callosum of control P60 male mice, in line with previous studies (Wild et al. 2022; Sjöstedt et al. 2020) (Dataset S1).

To determine potential mechanisms and pathways that are perturbed by *Zdhhc9* ablation, we completed PANTHER gene ontology (GO) enrichment analysis for biological processes on the differentially expressed genes. An analysis of downregulated genes revealed enrichment in numerous processes related to cholesterol and sterol metabolism and biosynthesis, whereas upregulated genes were enriched in pathways with the broad designation "signaling" (Figure 1c).

We next examined the relationships between our 173 differentially expressed genes using STRING (Search Tool for the Retrieval of Interacting Genes) protein–protein interaction network analysis (Figure S2). We identified two main clusters of genes with functions related to the immune system (highlighted in green) and cholesterol metabolism (highlighted in orange). The immune cluster included genes associated with microglia (such as *Ctss*, *C1qa*, *Ly86*, *Laptm5*, *Csf1r*; Figures 1b and S2). Most genes in these clusters were downregulated, suggesting a potential impairment in both immune regulation and cholesterol metabolism in *Zdhhc9*-KO mice.

We next performed quantitative reverse transcriptase polymerase chain reaction (qRT-PCR) on six selected genes that were identified in key signaling networks in our PANTHER and STRING RNAseq analysis, including myelin formation (*Mobp*), myelin assembly (*Pmp22*), glial cell differentiation (*Hapln2*), lipid transport (*Apod*, *Slco3a1*) and lipid metabolism (*Ldlr*). We confirmed decreased expression of all six genes in line with our RNAseq data, supporting the robustness of our dataset (Figure 1d).

Changes in gene expression observed in bulk RNAseq data can be attributed to a variety of factors, including differential gene transcription within cells and variations in cell type proportions. We noted that several differentially expressed genes in *Zdhhc9*-KO mice were marker genes for mature oligodendrocytes (*Hapln2*, *Apod*, *Trf*) (Marques et al. 2016), indicating potential changes in oligodendrocyte cell type proportions. We therefore proceeded to investigate whether the genes exhibiting differential expression in the corpus callosum of *Zdhhc9*-KO mice were expressed in distinct oligodendrocyte subtypes. This was done by analyzing cell-type expression patterns using the latest comprehensive scRNA sequencing study of the adult (P60) mouse brain, conducted by the Allen Institute (Zeisel et al. 2018). Gene expression Z-scores were plotted for each oligodendrocyte subtype, with a high Z-score indicating enrichment within a particular cell type. We found that most genes that were up-regulated in *Zdhhc9*-KO mice were enriched in OPCs, while most down-regulated genes were enriched in MOL2/3 cells (Figure 1e). These results indicate that changes in gene expression might be in part due to changes in the subtype proportions of oligodendrocyte lineage cells.

To further investigate potential changes in oligodendrocyte cell type proportions, we used a bioinformatic bulk-RNAseq deconvolution method, Bisque, to estimate the cell type proportions in the corpus callosum of control and *Zdhhc9*-KO mice. Bisque analysis utilizes scRNA-seq data to generate a reference gene expression profile that can be applied to approximate cell subtype proportions within a bulk RNAseq sample (Jew et al. 2020). We utilized the scRNAseq study of the adult (P60) mouse brain from the Allen Institute as a reference dataset for Bisque (Yao et al. 2023). This analysis revealed an increase in OPCs and a decrease in MOL2/3 cells in *Zdhhc9*-KO mice (Figure 1f), mirroring our observation that upregulated genes are enriched in OPCs and downregulated genes are enriched in MOL2/3 cells (Figure 1e). Interestingly, we also observed an increase in the MOL5/6 subtype in *Zdhhc9*-KO mice (Figure 1f). This estimation of MOL5/6 may be influenced by the highly significant increased expression of *Svep1* (Figure 1b), a gene with highly enriched expression in the MOL6 subtype (Marques et al. 2016). These results point to potential changes in oligodendrocyte subtype proportions in the corpus callosum.

We also performed RNAseq on two additional micro-dissected brain regions, including the primary visual cortex, in which seizure activity is present in *Zdhhc9*-KO mice (Shimell et al. 2019), and the optic nerve (Figure S3a,b), another large white matter tract. Although we did not identify any differentially expressed genes in the visual cortex, we identified 21 significantly downregulated and 14 significantly upregulated genes in the optic nerve of *Zdhhc9*-KO animals (Figure S3b; Dataset S3). Analysis of gene expression across oligodendrocyte subtypes revealed an enrichment of downregulated genes in the MOL2/3 subtype, as observed in the corpus callosum (Figure S3c; Dataset S3). Notably, five genes were significantly downregulated in both the corpus callosum and optic nerve (*Apln*, *Selenop*, *Slc45a3*, *Pmp22 and S100b*) (Figure S3d). Among these, four genes (*Apln*, *Selenop*, *Slc45a3* and *Pmp22*)

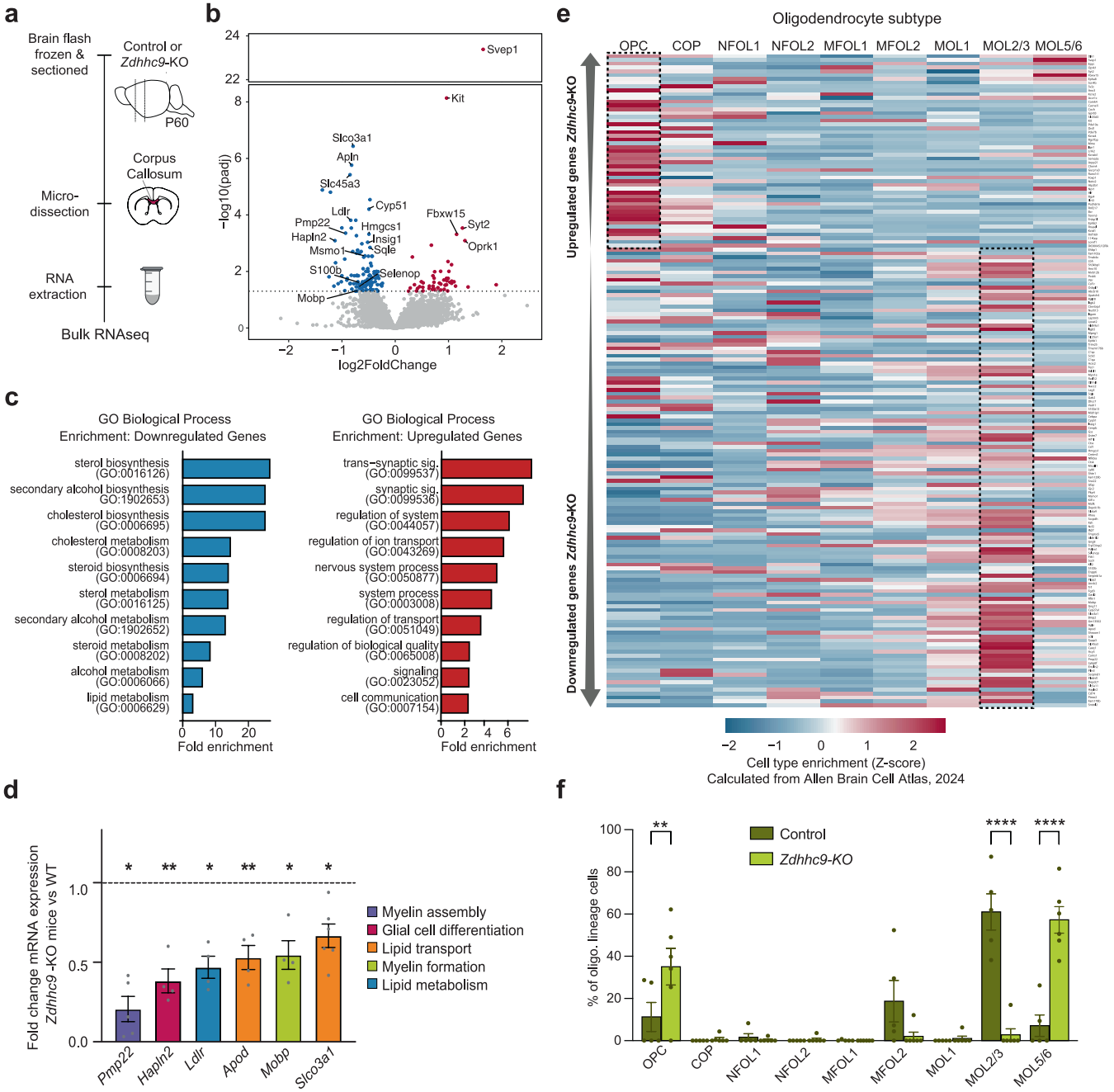

FIGURE 1 | There is a change in mature oligodendrocyte gene expression and genes involved in lipid metabolism in the corpus callosum of *Zdhhc9*-KO mice. (a) Illustration showing pipeline for RNAseq analysis in P60 mice. (b) Quantification of fold change in gene expression ($n = 5$ *Zdhhc9*-KO mice, $n = 6$ control mice). Each point represents an individual gene; blue denotes genes that are downregulated, and red denotes genes that are upregulated in *Zdhhc9*-KO mice relative to controls. The horizontal line denotes the statistical significance threshold required for two tailed *t*-tests; *p*-values were adjusted to account for multiple comparisons. Top 5 downregulated and upregulated genes are annotated, along with genes of interest. (c) Enrichment analysis for Biological Process GO terms for both up- and downregulated genes. The 10 GO terms with largest fold enrichment based on FDR value are shown. (d) Graph of RT-qPCR data for a subset of differentially expressed genes with known roles in myelination ($n = 4$–6 *Zdhhc9*-KO mice, $n = 4$–6 control mice). Normalized expression of each gene relative to control (dotted line). (e) Heatmap showing the expression of the 173 differentially expressed genes in *Zdhhc9*-KO mice across various oligodendrocyte subtypes, as derived from single-cell RNA sequencing data from the Allen Brain Cell (ABC) Atlas. Genes are listed (top to bottom) by decreasing $\log_2$ Fold change, ranging from the most upregulated to the most downregulated. Dotted black boxes highlight predominant cell type enrichment of upregulated and downregulated genes. (f) Bisque bioinformatic estimation of oligodendrocyte cell type proportions in the corpus callosum, performed on bulk RNAseq data from this study and using Allen brain ABC atlas as a reference scRNAseq dataset.

are most highly expressed in the MOL2/3 cell type relative to other oligodendrocyte subtypes and are known to be involved in oligodendrocyte differentiation and/or myelination (Shin et al. 2012; Ito et al. 2021; Chavali et al. 2020; Jouaud et al. 2019). Bisque approximation of cell type proportions again revealed a significant decrease in the MOL2/3 subtype

of oligodendrocytes in the optic nerve, indicating a decrease in the MOL2/3 subtype is common to both white matter tracts (Figure S3e). The shared alterations in gene expression observed in both the corpus callosum and optic nerve suggest a common pattern of altered gene expression following *Zdhhc9* loss that affects multiple white matter tracts in the brain.

3.3 | Altered Oligodendrocyte Subtype Proportions in *Zdhhc9*-KO Mice

The changes in gene expression identified with RNAseq predict alterations in the proportion of oligodendrocyte lineage cells in *Zdhhc9*-KO mice (Figure 1d). We therefore designed fluorescent in situ hybridization (FISH RNAscope) probes for the dominant MOL subtypes in the corpus callosum, guided by expression data from previously published scRNAseq and FISH studies (Marques et al. 2016; Yao et al. 2023; Zeisel et al. 2018) (Figure S4a). We chose marker genes with highly enriched expression in specific oligodendrocyte lineage cell subtypes, including *Hapln2* (MOL2/3 marker), *Ptgds* (MOL5/6 marker), and *C030029H02Rik* (MOL5/6 marker, Figure S4a). Importantly, within each cell type identified, we found no difference in the mean FISH probe coverage of each marker gene in control vs. *Zdhhc9*-KO mice, confirming that these marker genes can be used to infer changes in cell number (Figure S4b). In line with our Bisque deconvolution analysis, there was a decrease in the proportion of MOL2/3 cells, with a concomitant increase in the proportion of MOL5/6 cells in the corpus callosum of *Zdhhc9*-KO mice (Figure 2a–c).

We next directly quantified whether the density of OPCs or intermediate maturity oligodendrocytes was altered in *Zdhhc9*-KO mice using a second set of FISH probes including *Pdgfra* (OPC marker), *Itpr2* (NFOL marker) and *Ctps* (MFOL marker) (Figure S4a). While we observed no changes in the density of intermediate maturity oligodendrocyte lineage cells, we observed an increase in the density of OPCs, in line with data in Figure 1F (Figure 2d–f). The increase in OPC density in *Zdhhc9*-KO mice may reflect an intrinsic failure of OPC differentiation or a compensatory increase in OPC proliferation and/or migration into the corpus callosum in response to a decreased MOL2/3 population. We also observed no change in the density of oligodendrocyte lineage cells ($Olig2^+$) or mature oligodendrocytes ($Olig2^+/CC1^+$) in the corpus callosum of *Zdhhc9*-KO mice (Figure 2g,h). Together, our analysis of differential expression, Bisque deconvolution, and FISH data all corroborate alterations in the subtype proportions of oligodendrocyte lineage cells in the corpus callosum of *Zdhhc9*-KO mice. This includes a reduction in the MOL2/3 subtype, which notably expresses genes linked to myelination, and an increase in OPCs and the MOL5/6 subtype.

3.4 | No Changes in Density of Microglia, Astrocytes, Proliferative, or Apoptotic Oligodendrocytes in *Zdhhc9*-KO Mice

Previous studies have ascertained that astrocytes and microglia play an important role in myelination (Kıray et al. 2016; Hagemeyer et al. 2017; Santos and Fields 2021). We observed no changes in GFAP (marker for astrocyte) or Iba1 (marker for microglia) immunostaining in the corpus callosum, indicating that the observed deficits in myelination in *Zdhhc9*-KO mice were not caused by increased astrocyte or microglial activity at this time point (Figure S5a,b). We also observed no changes in Olig2/Ki67 and Olig2/CC3 immunostaining, demonstrating that differences in oligodendrocyte populations in the corpus callosum are not the result of altered proliferation or apoptosis in oligodendrocyte lineage cells (Figure S5c–f). Together, these data support the role of *Zdhhc9* in myelination and regulation of oligodendrocyte subtype proportions independent of proliferative or apoptotic responses in oligodendrocytes.

3.5 | Fewer Myelinated Axons and Myelin Compaction Abnormalities in the Corpus Callosum of *Zdhhc9*-KO Mice

We next completed ultrastructural analyses of the corpus callosum using Transmission Electron Microscopy (TEM) on sagittal brain sections of P60–100 male mice. While we observed no difference in total axon density (myelinated and unmyelinated axons) in the dorsal region of the corpus callosum sampled (Figure 3a,b), there was a significant reduction in the number of myelinated axons in *Zdhhc9*-KO mice (Figure 3a,c). This aligns with a reduction in the density of full nodes of Ranvier in the corpus callosum (Figure S6a–c). In contrast to unmyelinated axons, which had no significant difference in axon diameter (Figure 3a,d), the diameter of myelinated axons is larger in Zdhhc9-KO mice (Figure 3a,e). This is due to fewer small caliber axons being myelinated (Figure 3a,f). There is also an average increase in the g-ratio of myelinated axons in *Zdhhc9*-KO mice (Figure 3g) suggesting an overall hypomyelination of axons in these mice. A plot of g-ratio versus axon diameter further demonstrates significant differences in the slope of the linear regression lines, demonstrating hypomyelination of smaller caliber axons and hypermyelination of larger caliber axons in *Zdhhc9*-KO mice (Figure 3h). Analysis of the ultrastructure of myelinated axons demonstrated a significant increase in the number of axons with myelin abnormalities (Figure 3i, arrowheads in 3a), resembling the myelin loops seen in other mouse lines with myelin compaction issues (Bull et al. 2014). Further analyses showed increased distance between intraperiod and major dense lines (increased periodicity), suggesting myelin compaction deficits in *Zdhhc9*-KO mice (Figure 3j).

3.6 | Decreased Expression of Integral Myelin Proteins in the Myelin Proteome of *Zdhhc9*-KO Mice

To better understand how ablation of *Zdhhc9* can impact myelin integrity and compaction, we looked for changes in the myelin proteome using mass spectrometry. We isolated myelin from the whole brain of P23 male mice, an age corresponding with peak myelinogenesis (Sturrock 1980) and peak expression of Zdhhc9 (Wild et al. 2022) (Figure 4a). Whole brains were used as patients with XLID and *ZDHHC9* LOF mutations exhibit white matter reductions throughout the brain, including the corpus callosum, temporal lobes, optic nerve, and pituitary stalk (Baker et al. 2015). 79.6% of all identified proteins were detected in at least three of four control samples Dataset (S4, Figure S7a), and

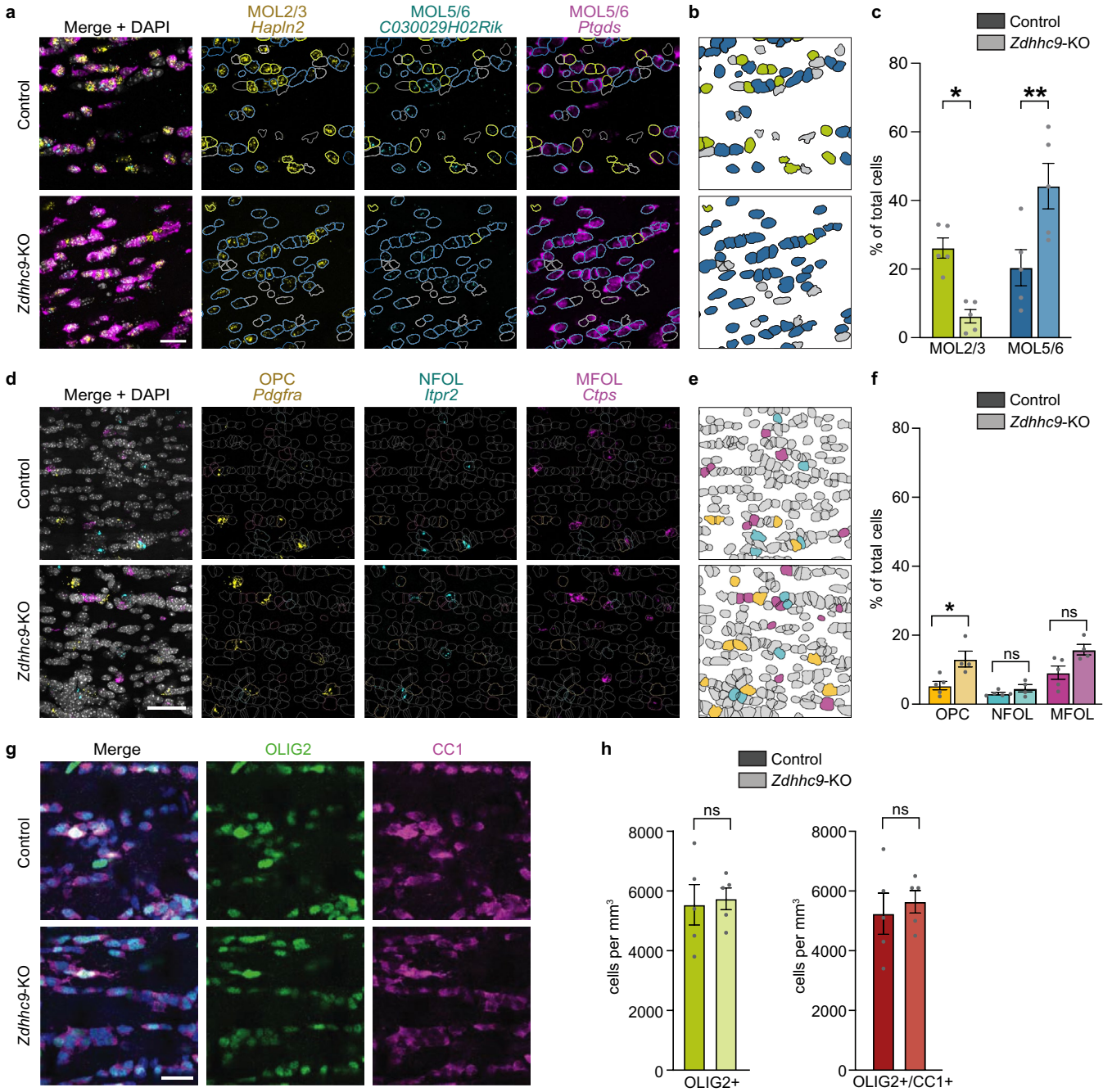

FIGURE 2 | There is a change in mature oligodendrocyte subtype densities, and an increase in the density of OPCs in the corpus callosum of *Zdhhc9*-KO mice. (a) Representative images of fluorescent in situ hybridization for MOL2/3 and MOL5/6 (*Hapln2*—MOL2/3; *C030029H02Rik*—MOL5/6; *Ptgds*—MOL5/6) in the P60 corpus callosum (scale bar, 50 μm) (b) Representative image of corpus callosum cells colored by oligodendrocyte subtype classification. MOL2/3 cells are colored green; MOL5/6 cells are colored blue; unclassified cells are colored gray. c Graph of oligodendrocyte subtype proportions ($n = 5$ mice per genotype). (d) Representative images of fluorescent in situ hybridization for immature oligodendrocyte cell-lineage-subtype marker genes (*Pdgfra*-OPCs, *Itpr2*-NFOLs, *Ctps*-MFOLs) in the corpus callosum (scale bar, 50 μm). (e) Representative image of corpus callosum cells colored by oligodendrocyte subtype classification. OPC cells are colored yellow; NFOL cells are colored cyan; MFOL cells are colored magenta; unclassified cells are colored gray. (f) Graph of OPC, NFOL and MFOL proportions ($n = 4$ *Zdhhc9*-KO mice, $n = 5$ control mice). (g) Representative images of OLIG2 (pan oligodendrocyte marker) and CC1 (mature oligodendrocyte marker) immunolabeling in the P60 corpus callosum. h Graph of OLIG2+ and OLIG2+/CC1+ proportions ($n = 5$ mice per genotype). Data in (c, f, h) show mean ± SEM. (c, f, h) multiple *t*-tests using Holm-Sidak method, alpha = 0.05.

77% of all proteins were detected in at least 3 of 4 *Zdhhc9*-KO samples Dataset (S4, Figure S7b). Of these, 90.8% (1864) of all proteins were identified in both genotypes Dataset (S4, Figure S7c). We observed significant differences in the myelin proteome, with an increase in 84 proteins and a decrease in 113 proteins in *Zdhhc9*-KO mice (Figure 4b). Interestingly, GOLGA7, ZDHHC9's co-factor, was the most significantly decreased protein (Figure 4b). Of the top 15 most abundantly expressed myelin proteins, four were significantly decreased in *Zdhhc9*-KO mice (Figure 4c). This included proteins that regulate myelin

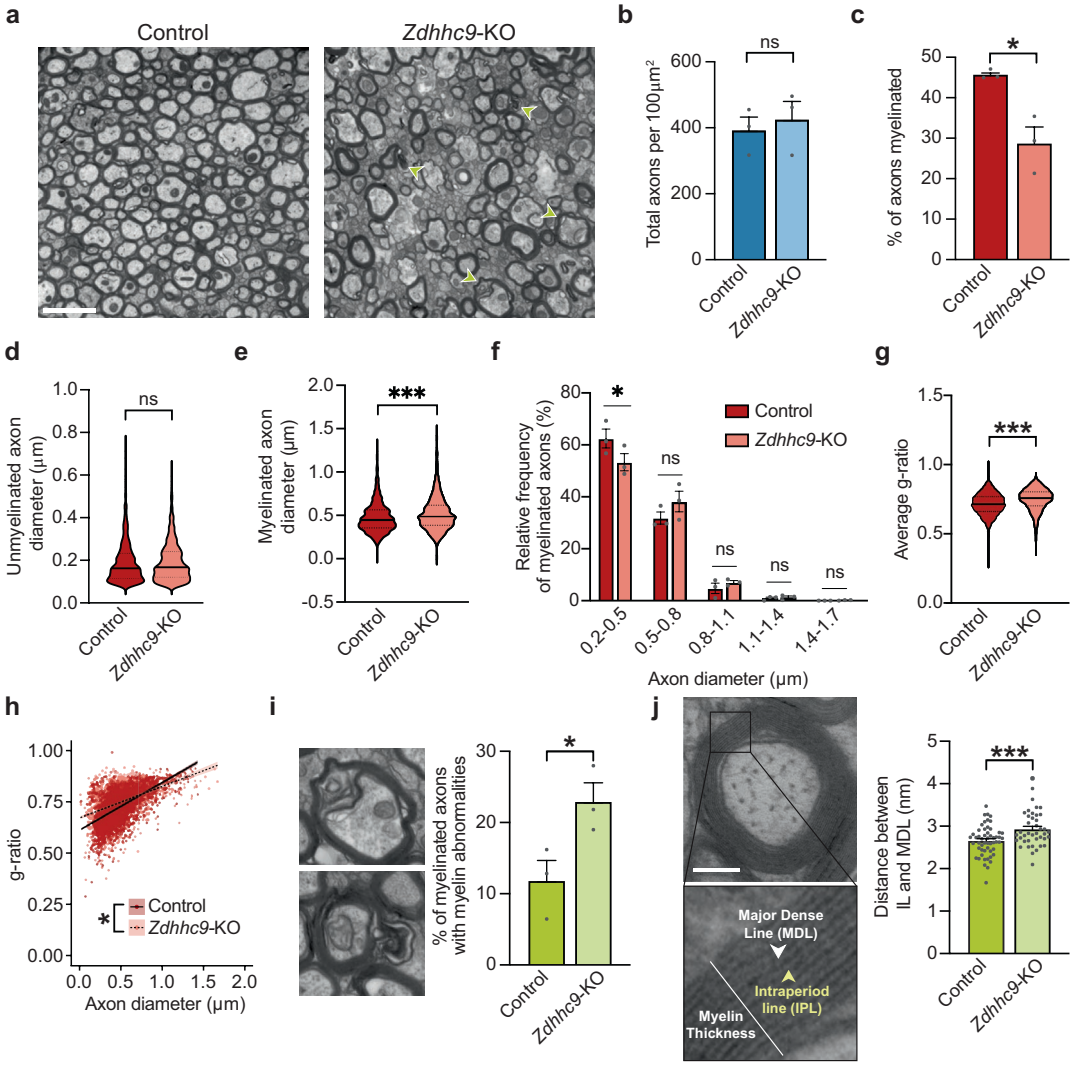

FIGURE 3 | There are fewer myelinated axons and decreased myelin compaction in the corpus callosum of *Zdhhc9*-KO mice. (a) Representative transmission electron microscopy images of the P60 corpus callosum (scale bar, 2 mm). (b) Quantification of axon density and (c) the percentage of axons that are myelinated ($n = 3$ mice per genotype). (d) The average diameter of unmyelinated axons ($n > 1000$ axons from 3 mice per genotype). (e) The average diameter of myelinated axons ($n > 1000$ axons from 3 mice per genotype). (f) Frequency distribution graph showing the relative frequency of myelinated axons with a given axon diameter ($n > 1000$ axons from three mice per genotype). (g) The average g-ratio of myelinated axons ($n > 1000$ axons from 3 mice per genotype). (h) Scatter plot of g-ratio versus axon diameter. i Representative images (left) and quantification (right) of axons with myelination decompaction phenotypes (myelin "loops") (scale bar, 1 mm). (j) Representative images of a myelinated axon, showing major dense line (MDL) and intraperiod line (IL) within the myelin sheath (scale bar, 100 nm) (left) and quantification of the average distance between IL and MDL ($n > 30$ axons from 3 mice per genotype). Data in (b, c, d, e, f, g, i, j) show mean ± SEM. (b, c, d, e, i, j) unpaired two-tailed Student's *t*-tests; (d, g) Welch's *t*-test; (h) Type II Sum of Squares Analysis of Covariance (ANCOVA).

compaction (CLDN11, MOBP, SIRT2) (Riedhammer et al. 2021; Yoshikawa 2001; Beirowski et al. 2011; Werner et al. 2007), and one protein that has been shown to regulate oligodendrocyte differentiation and the maintenance of mature myelin (MAG) (Quarles 2007). GO term annotation of the 197 differentially expressed proteins showed an association with 25 different biological processes, including axon ensheathment, lipid binding, and lipid metabolism (Dataset S5, Figure 4d).

Interestingly, ZDHHC9 was the only palmitoyl acyl transferase detected in isolated myelin, suggesting a crucial role for this enzyme in regulating the dynamic palmitoylation of myelin proteins within the myelin sheath. Four depalmitoylating enzymes in the ABHD family of palmitoyl thioesterases were identified in control myelin, and of these, two (ABHD4 and ABHD17B) were significantly reduced in *Zdhhc9*-KO mice (Figure 4e). We validated the proteomics results using western blot analysis (Figure 4f), again showing a significant decrease in CLDN11, SIRT2, and MOBP protein levels, with no change in MBP and MOG (Figure 4f,g). Overall, these data reveal substantial changes in the composition of the myelin proteome in *Zdhhc9*-KO mice that may underlie the dysmyelination phenotypes observed with EM.

4 | Discussion

This study highlights an important role for ZDHHC9 in the proper development of oligodendrocyte lineage cells and axon

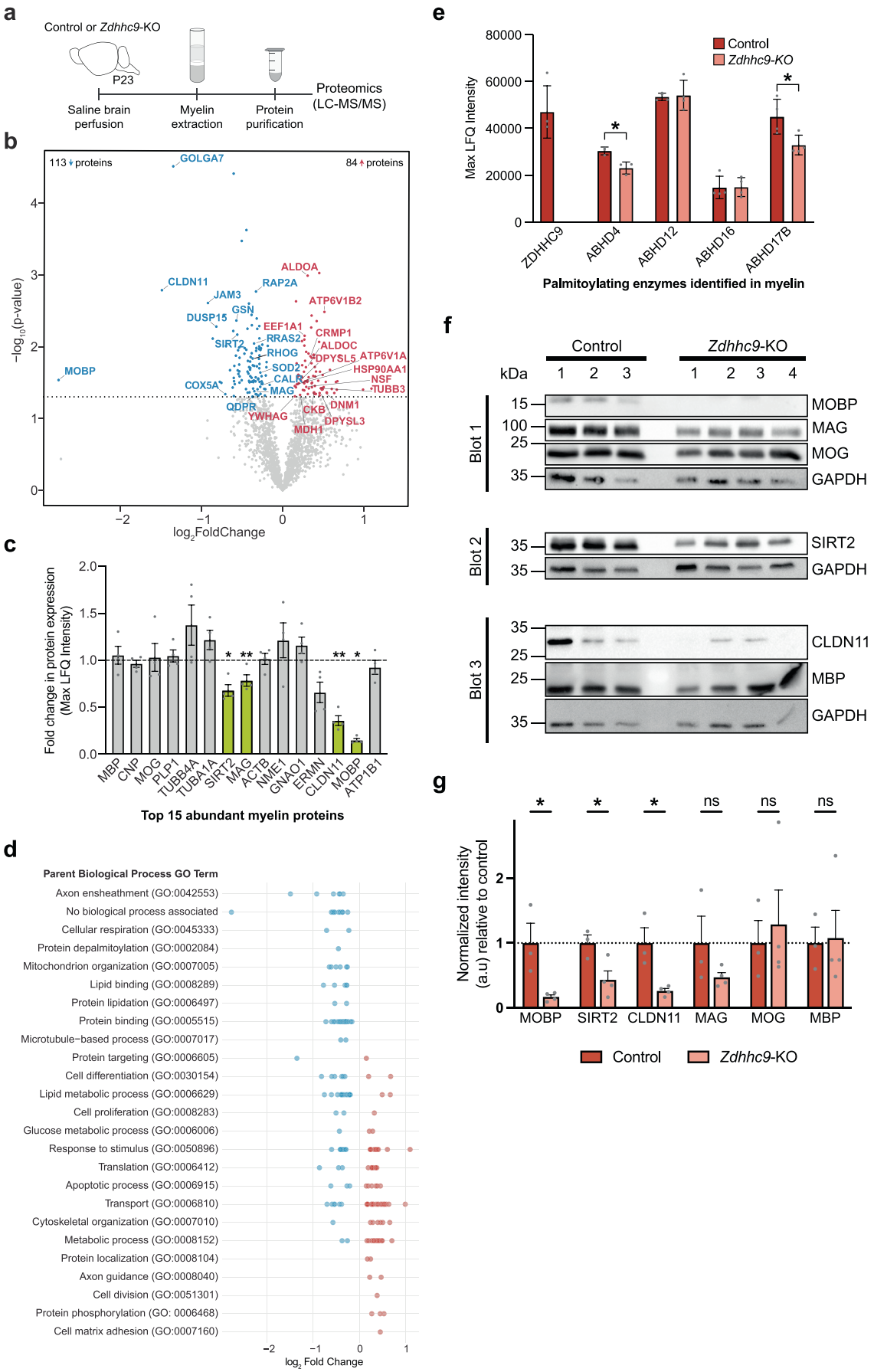

FIGURE 4 | Legend on next page.

FIGURE 4 | Proteins associated with myelination and myelin compaction are decreased in *Zdhhc9*-KO mice. (a) Illustration showing the pipeline for myelin proteomic analysis of P23 mice. (b) Quantification of fold change in protein expression ($n = 4$ mice per genotype). Each point represents an individual protein; blue denotes proteins that are downregulated, and red denotes proteins that are upregulated in *Zdhhc9*-KO mice relative to controls. The horizontal line denotes the statistical significance threshold required for two tailed t-tests. Labeled proteins denote those that are both differentially expressed and highly abundant (top 10% of control myelin proteome). (c) Graph of Max LFQ Intensity data for the 15 most abundant myelin proteins ($n = 4$ mice per genotype). Normalized expression of each protein relative to control (dotted line). Differentially expressed proteins are highlighted in green. (d) Graph of the biological process GO Term associated with each differentially expressed protein along with their $\log_2$ Fold Change. (e) Graph of Max LFQ Intensity data for all palmitoylating enzymes identified in myelin ($n = 4$ mice per genotype). f Western blots used to validate proteomics results. (g) Quantification of changes in myelin protein levels as determined by western blot. ($n = 3$ control mice; $n = 4$ *Zdhhc9*-KO mice). All statistical analyses were done using unpaired two-tailed Student's *t*-tests.

myelination within the corpus callosum. *Zdhhc9* ablation disrupts the balance of mature oligodendrocyte subtypes, leading to an increase in MOL5/6 cells and a corresponding decrease in MOL2/3 cells. Since MOL2/3 cells are transcriptionally enriched for genes associated with myelination, their reduction likely accounts for the overall decrease in the number of myelinated axons in the corpus callosum of *Zdhhc9* KO mice. Using RNAseq and proteomic analyses, we identified multiple signaling pathways and key regulatory proteins that are involved in oligodendrocyte maturation, offering mechanistic insights into altered subtype proportions. Additionally, we demonstrate that loss of *Zdhhc9* impairs myelin integrity and compaction, indicating disrupted oligodendrocyte function. The observed reduction in key myelin proteins essential for myelin structure and compaction provides a mechanistic explanation for these defects.

Previous studies have demonstrated that ZDHHC enzymes modulate gene expression through the palmitoylation of transcription factors, chromatin remodelers (Chen et al. 2017, 2014, 2016), and histones (Zou et al. 2011; Wilson et al. 2011). Thus, the altered gene expression observed in the corpus callosum of *Zdhhc9*-KO mice may also be due to changes in the palmitoylation of these substrates as well as signaling pathways that alter gene transcription. Notably, in our dataset, we identified altered expression of several genes encoding proteins that further regulate gene expression. For example, we observed decreased expression of *Insig1*, a modulator of sterol regulatory element-binding proteins (SREBPs) (Gong et al. 2006), which are key regulatory transcription factors for lipid metabolism and synthesis (Eberlé et al. 2004). The decreased expression we observed in a large cluster of genes involved in cholesterol metabolism is particularly interesting given that cholesterol is the only essential lipid in myelin membranes (Saher and Stumpf 2015) and is known to regulate the extent of myelination (Saher et al. 2005; Mathews and Appel 2016), influence myelin compaction (Saher et al. 2011), and act as a signaling molecule to drive oligodendrocyte differentiation and maturation (Montani 2021).

In oligodendrocyte lineage cells, *Zdhhc9* is initially detected in NFOLs, peaks in MFOLs, and then maintains an intermediate expression level in the six MOL subtypes (Marques et al. 2016). One possible mechanism by which *Zdhhc9* ablation may alter MOL subtype proportions is through the loss of palmitoylation of proteins essential for the maturation of oligodendrocytes beyond the NFOL stage. For example, *Zdhhc9*-KO mice exhibit downregulation of SIRT2, which has been shown to deacetylate the H3K18 histone and disinhibit the transcription of myelin genes such as *Mbp*, thereby promoting oligodendrocyte differentiation and development (Ma et al. 2022). Another downregulated protein in *Zdhhc9*-KO mice, MAG, has been shown to promote oligodendrocyte maturation through ANTGPTL2 signaling, which transactivates the myelin regulatory factor (MYRF) (Chen et al. 2023). Although the mechanism is not yet understood, ablation of *S100b*, another downregulated gene in *Zdhhc9*-KO mice, has been shown to delay the morphological transformation and maturation of oligodendrocytes (Deloulme et al. 2004).

In addition to changes in MOL subtype proportions, there was a marked increase in the density of OPCs in the corpus callosum of KO mice. Expression of *Zdhhc9* in OPCs is low, making it unlikely that the increase in the OPC population in *Zdhhc9*-KO mice is due to a failure of OPC differentiation. Alternatively, we propose that the increase in OPC density reflects a compensatory mechanism to repopulate depleted mature oligodendrocytes and/or a response to the decrease in myelinated axons (Levine and Reynolds 1999).

The importance of maintaining a balanced proportion of MOL subtypes is underscored by alterations in MOL subtype proportions across various myelin disease states (Pandey et al. 2022; Jäkel et al. 2019). In patients with multiple sclerosis, failure to remyelinate is correlated with fewer MOL2/3 cells and more MOL5/6 cells (Jäkel et al. 2019). Furthermore, following cuprizone-induced demyelination in mice, remyelination is associated with (Thornton et al. 2024) an upregulation of MOL2/3 but not MOL5/6[77] oligodendrocytes77. Work in EAE mouse models for multiple sclerosis suggests that MOL2/3 oligodendrocytes may be more prone to dying; to date, it is unclear why (Kukanja et al. 2024). Interestingly, PLP-KO mice show a similar phenotype to *Zdhhc9*-KO mice, with fewer myelinated axons (Rosenbluth et al. 2006), reduced myelin compaction (Rosenbluth et al. 2006), a decrease in MOL2/3, and an increase in MOL5/6 cells (Sun 2022). Further work is needed to determine the functional distinctions between the different MOL subtypes and to identify the underlying mechanisms driving changes in MOL subtype proportions during pathological conditions.

Palmitoylation of myelin proteins can influence their stability and proper targeting to subcellular compartments (Schneider et al. 2005). While approximately 20% of the entire proteome are substrates for palmitoylation (Miles et al. 2021), a striking 94% of myelin proteins can be palmitoylated (Jahn et al. 2020; Blanc et al. 2015) suggesting an important role for palmitoylation in myelin. Notably, we identify ZDHHC9 as the sole palmitoylating enzyme in whole brain myelin, positioning it as a

key regulator of myelin palmitoylation. We observed reductions in MOBP and CLDN11, key myelin proteins found in compact myelin (Yamamoto et al. 1994). Both MOBP and CLDN11 have been identified as palmitoylation substrates in palmitoylproteome studies (Blanc et al. 2015; Arroyo and Scherer 2000), and MOBP has been previously shown to be directly palmitoylated by ZDHHC9 (Wild et al. 2022). However, it is not clear whether ZDHHC9-mediated palmitoylation of these proteins is important for their stability or for their insertion into the myelin sheath. Interestingly, patients with *CLDN11* loss-of-function mutations exhibit hypomyelination in the brain, including in the corpus callosum (Riedhammer et al. 2021).

Our myelin proteomics analysis also revealed a decrease in the protein levels of two other palmitoylated proteins (Blanc et al. 2015), SIRT2 and MAG. Both *Sirt2*-KO and *Mag*-KO mice exhibit delayed initiation of developmental myelination (Beirowski et al. 2011; Schachner and Bartsch 2000; Bartsch et al. 1997; Montag et al. 1994). Furthermore, *Mag* ablation significantly delays myelin compaction, with *Mag*-KO mice showing a higher incidence of myelin abnormalities, including myelin loops (Quarles 2007). Similarly, *Sirt2*-KO mice exhibit impaired remyelination and produce thinner and looser new myelin (Ma et al. 2022). The changes in protein and gene expression observed in *Zdhhc9*-KO mice altogether indicate an overall disruption in biological pathways important for oligodendrocyte maturation and myelin formation.

Overall, we propose a model for decreased myelination in the corpus callosum of *Zdhhc9*-KO mice that is a result of (i) changes in the proportions of oligodendrocyte lineage cells and (ii) decreased expression of numerous proteins that are involved in cholesterol biosynthesis and maintaining myelin integrity. The findings of this study establish a critical role for ZDHHC9 in oligodendrocyte development and myelination and identify dysregulated signaling pathways that may underlie the decrease in white matter volume, epileptic comorbidities, and intellectual disability seen in patients with *ZDHHC9* mutations.

Author Contributions

Experimental design conceptualization, S.X.B., A.R.W., T.P.O., R.B.W.; data generation, R.B.W., A.R.W., T.P.O., A.J.T., A.P., J.C.R., M.M., N.D.; data analysis, R.B.W., A.R.W., T.P.O., A.J.T., S.F., J.C.R.; Figure creation, R.B.W., A.R.W., T.P.O., A.J.T., S.X.B.; manuscript writing, R.B.W., A.R.W., T.P.O., A.J.T., and S.X.B.

Acknowledgments

The authors thank Drs. Gareth Thomas and Shin Hyeok Kang (Temple University) for insightful discussions throughout the study. We thank the UBC Proteomic Core as well as Dr. Naoji Yubuki, the UBC Bioimaging Facility (RRID: SCR_021304) and the UBC School of Biomedical Engineering Sequencing Core at the Biomedical Research Center for technical help. Dr. Mark Cembrowski's lab (UBC) provided expertise on FISH. This work is supported by grants from CIHR (FDN-159907) (S.X.B.) and NIH (AWD-020422) (Gareth Thomas, Shin Hyeok Kang, and S.X.B.), as well as by computational resources made available through the NeuroImaging and NeuroComputation Centre at the Djavad Mowafaghian Centre for Brain Health (RRID:SCR_019086) and the Dynamic Brain Circuits in Health and Disease Research Excellence Cluster DataBinge Forum.

Disclosure

Preprint Servers: bioRxiv (https://doi.org/10.1101/2023.08.08.552342).

Conflicts of Interest

The authors declare no conflicts of interest.

Data Availability Statement

The data that support the findings of this study are openly available in Proteome Exchange at https://proteomecentral.proteomexchange.org/cgi/GetDataset?ID=PXD043437, reference number PXD043437.

References

Allimuthu, D., Z. Hubler, F. J. Najm, et al. 2019. "Diverse Chemical Scaffolds Enhance Oligodendrocyte Formation by Inhibiting CYP51, TM7SF2, or EBP." *Cell Chemical Biology* 26: 593–599.e4.

Arroyo, E. J., and S. S. Scherer. 2000. "On the Molecular Architecture of Myelinated Fibers." *Histochemistry* 113: 1.

Baker, K., D. E. Astle, G. Scerif, et al. 2015. "Epilepsy, Cognitive Deficits and Neuroanatomy in Males With ZDHHC9 Mutations." *Annals of Clinical Translational Neurology* 2: 559–569.

Baldarelli, R. M., C. M. Smith, J. H. Finger, et al. 2021. "The Mouse Gene Expression Database (GXD): 2021 Update." *Nucleic Acids Research* 49: D924–D931.

Bartsch, S., D. Montag, M. Schachner, and U. Bartsch. 1997. "Increased Number of Unmyelinated Axons in Optic Nerves of Adult Mice Deficient in the Myelin-Associated Glycoprotein (MAG)." *Brain Research* 762, no. 1-2: 231–234.

Bathelt, J., D. Astle, J. Barnes, F. L. Raymond, and K. Baker. 2016. "Structural Brain Abnormalities in a Single Gene Disorder Associated With Epilepsy, Language Impairment and Intellectual Disability." *NeuroImage: Clinical* 12: 655–665.

Beirowski, B., J. Gustin, S. M. Armour, et al. 2011. "Sir-Two-Homolog 2 (Sirt2) Modulates Peripheral Myelination Through Polarity Protein Par-3/Atypical Protein Kinase C (aPKC) Signaling." *Proceedings. National Academy of Sciences. United States of America* 108: E952–E961.

Blanc, M., F. David, L. Abrami, et al. 2015. "SwissPalm: Protein Palmitoylation Database." *F1000Res* 4: 261.

Boone, P. M., C. A. Bacino, C. A. Shaw, et al. 2010. "Detection of Clinically Relevant Exonic Copy-Number Changes by Array CGH." *Human Mutation* 31: 1326–1342.

Bray, N. L., H. Pimentel, P. Melsted, and L. Pachter. 2016. "Near-Optimal Probabilistic RNA-seq Quantification." *Nature Biotechnology* 34: 525–527.

Bull, S.-J., J. M. Bin, E. Beaumont, et al. 2014. "Progressive Disorganization of Paranodal Junctions and Compact Myelin due to Loss of DCC Expression by Oligodendrocytes." *Journal of Neuroscience* 34: 9768–9778.

Carpenter, A. E., T. R. Jones, M. R. Lamprecht, et al. 2006. "CellProfiler: Image Analysis Software for Identifying and Quantifying Cell Phenotypes." *Genome Biology* 7: R100.

Chamberlain, L. H., and M. J. Shipston. 2015. "The Physiology of Protein *S*-Acylation." *Physiological Reviews* 95: 341–376.

Chan, Q. W. T., C. G. Howes, and L. J. Foster. 2006. "Quantitative Comparison of Caste Differences in Honeybee Hemolymph." *Molecular & Cellular Proteomics* 5: 2252–2262.

Chavali, M., M. J. Ulloa-Navas, P. Pérez-Borredá, et al. 2020. "Wnt-Dependent Oligodendroglial-Endothelial Interactions Regulate White Matter Vascularization and Attenuate Injury." *Neuron* 108: 1130–1145.e5.

Chen, L., Z. Yu, L. Xie, et al. 2023. "ANGPTL2 Binds MAG to Efficiently Enhance Oligodendrocyte Differentiation." *Cell & Bioscience* 13: 42.

Chen, X., Z. du, X. Li, et al. 2016. "Protein Palmitoylation Regulates Neural Stem Cell Differentiation by Modulation of EID1 Activity." *Molecular Neurobiology* 53: 5722–5736.

Chen, X., Z. du, W. Shi, et al. 2014. "2-Bromopalmitate Modulates Neuronal Differentiation Through the Regulation of Histone Acetylation." *Stem Cell Research* 12: 481–491.

Chen, X., H. Ma, Z. Wang, S. Zhang, H. Yang, and Z. Fang. 2017. "EZH2 Palmitoylation Mediated by ZDHHC5 in p53-Mutant Glioma Drives Malignant Development and Progression." *Cancer Research* 77: 4998–5010.

Codeluppi, S., L. E. Borm, A. Zeisel, et al. 2018. "Spatial Organization of the Somatosensory Cortex Revealed by osmFISH." *Nature Methods* 15: 932–935.

Collins, M. O., K. T. Woodley, and J. S. Choudhary. 2017. "Global, Site-Specific Analysis of Neuronal Protein S-Acylation." *Scientific Reports* 7: 4683.

Deloulme, J. C., E. Raponi, B. J. Gentil, et al. 2004. "Nuclear Expression of S100B in Oligodendrocyte Progenitor Cells Correlates With Differentiation Toward the Oligodendroglial Lineage and Modulates Oligodendrocytes Maturation." *Molecular and Cellular Neuroscience* 27: 453–465.

Du, C., Y. Duan, W. Wei, et al. 2016. "Kappa Opioid Receptor Activation Alleviates Experimental Autoimmune Encephalomyelitis and Promotes Oligodendrocyte-Mediated Remyelination." *Nature Communications* 7: 11120.

Eberlé, D., B. Hegarty, P. Bossard, P. Ferré, and F. Foufelle. 2004. "SREBP Transcription Factors: Master Regulators of Lipid Homeostasis." *Biochimie* 86: 839–848.

Erwig, M. S., K. Kusch, S. Tenzer, O. Jahn, and H. B. Werner. 2019. "Myelin: Methods for Purification and Proteome Analysis." *Methods in Molecular Biology* 27.

Floriddia, E. M., T. Lourenço, S. Zhang, et al. 2020. "Distinct Oligodendrocyte Populations Have Spatial Preference and Different Responses to Spinal Cord Injury." *Nature Communications* 11: 5860.

Franklin, K. B. J., and G. Paxinos. 2008. *The Mouse Brain in Stereotaxic Coordinates*. Elsevier.

Goeminne, L. J. E., K. Gevaert, and L. Clement. 2018. "Experimental Design and Data-Analysis in Label-Free Quantitative LC/MS Proteomics: A Tutorial With MSqRob." *Journal of Proteomics* 171: 23–36.

Gong, Y., J. N. Lee, P. C. W. Lee, J. L. Goldstein, M. S. Brown, and J. Ye. 2006. "Sterol-Regulated Ubiquitination and Degradation of Insig-1 Creates a Convergent Mechanism for Feedback Control of Cholesterol Synthesis and Uptake." *Cell Metabolism* 3: 15–24.

Grozeva, D., K. Carss, O. Spasic-Boskovic, et al. 2015. "Targeted Next-Generation Sequencing Analysis of 1,000 Individuals With Intellectual Disability." *Human Mutation* 36: 1197–1204.

Hagemeyer, N., K. M. Hanft, M. A. Akriditou, et al. 2017. "Microglia Contribute to Normal Myelinogenesis and to Oligodendrocyte Progenitor Maintenance During Adulthood." *Acta Neuropathologica* 134: 441–458.

Han, J. Y., J. H. Jang, J. Park, and I. G. Lee. 2018. "Targeted Next-Generation Sequencing of Korean Patients With Developmental Delay and/or Intellectual Disability." *Frontiers in Pediatrics* 6: 391.

Han, J. Y., I. G. Lee, S. Shin, M. Kim, J. H. Jang, and J. Park. 2017. "The First Patient With Sporadic X-Linked Intellectual Disability With de Novo ZDHHC9 Mutation Identified by Targeted Next-Generation Sequencing." *European Journal of Medical Genetics* 60: 499–503.

Hilscher, M. M., C. M. Langseth, P. Kukanja, C. Yokota, M. Nilsson, and G. Castelo-Branco. 2022. "Spatial and Temporal Heterogeneity in the Lineage Progression of Fine Oligodendrocyte Subtypes." *BMC Biology* 20: 122.

Hu, J., S.-. L. Fu, K.-. H. Zhang, et al. 2004. "Differential Gene Expression in Neural Stem Cells and Oligodendrocyte Precursor Cells: A cDNA Microarray Analysis." *Journal of Neuroscience Research* 78, no. 5: 637–646. https://doi.org/10.1002/jnr.20317.

Ito, M., R. Muramatsu, Y. Kato, et al. 2021. "Age-Dependent Decline in Remyelination Capacity Is Mediated by Apelin–APJ Signaling." *Nature Aging* 1: 284–294.

Jahn, O., S. B. Siems, K. Kusch, et al. 2020. "The CNS Myelin Proteome: Deep Profile and Persistence After Post-Mortem Delay." *Frontiers in Cellular Neuroscience* 14: 239.

Jäkel, S., E. Agirre, A. Mendanha Falcão, et al. 2019. "Altered Human Oligodendrocyte Heterogeneity in Multiple Sclerosis." *Nature* 566: 543–547.

Jew, B., M. Alvarez, E. Rahmani, et al. 2020. "Accurate Estimation of Cell Composition in Bulk Expression Through Robust Integration of Single-Cell Information." *Nature Communications* 11: 1971.

Jouaud, M., S. Mathis, L. Richard, A. S. Lia, L. Magy, and J. M. Vallat. 2019. "Rodent Models With Expression of PMP22: Relevance to Dysmyelinating CMT and HNPP." *Journal of the Neurological Sciences* 398: 79–90.

Kaiser, T., H. M. Allen, O. Kwon, et al. 2021. "MyelTracer: A Semi-Automated Software for Myelin *g*-Ratio Quantification." *eNeuro* 8, no. 4: ENEURO.0558-20.2021. https://doi.org/10.1523/ENEURO.0558-20.2021.

Kıray, H., S. L. Lindsay, S. Hosseinzadeh, and S. C. Barnett. 2016. "The Multifaceted Role of Astrocytes in Regulating Myelination." *Experimental Neurology* 283: 541–549.

Kong, A. T., F. V. Leprevost, D. M. Avtonomov, D. Mellacheruvu, and A. I. Nesvizhskii. 2017. "MSFragger: Ultrafast and Comprehensive Peptide Identification in Mass Spectrometry–Based Proteomics." *Nature Methods* 14: 513–520.

Kouskou, M., D. M. Thomson, R. R. Brett, et al. 2018. "Disruption of the Zdhhc9 Intellectual Disability Gene Leads to Behavioural Abnormalities in a Mouse Model." *Experimental Neurology* 308: 35–46.

Ku, R., and M. Torii. 2020. "New Molecular Players in the Development of Callosal Projections." *Cells* 10: 29.

Kukanja, P., C. M. Langseth, L. A. Rubio Rodríguez-Kirby, et al. 2024. "Cellular Architecture of Evolving Neuroinflammatory Lesions and Multiple Sclerosis Pathology." *Cell* 187: 1990–2009.e19.

Kvilekval, K., D. Fedorov, B. Obara, A. Singh, and B. S. Manjunath. 2010. "Bisque: A Platform for Bioimage Analysis and Management." *Bioinformatics* 26: 544–552.

Levine, J. M., and R. Reynolds. 1999. "Activation and Proliferation of Endogenous Oligodendrocyte Precursor Cells During Ethidium Bromide-Induced Demyelination." *Experimental Neurology* 160: 333–347.

Love, M. I., W. Huber, and S. Anders. 2014. "Moderated Estimation of Fold Change and Dispersion for RNA-Seq Data With DESeq2." *Genome Biology* 15: 550.

Ma, X.-R., X. Zhu, Y. Xiao, et al. 2022. "Restoring Nuclear Entry of Sirtuin 2 in Oligodendrocyte Progenitor Cells Promotes Remyelination During Ageing." *Nature Communications* 13: 1225.

Marques, S., A. Zeisel, S. Codeluppi, et al. 2016. "Oligodendrocyte Heterogeneity in the Mouse Juvenile and Adult Central Nervous System." *Science* 352: 1326–1329.

Masurel-Paulet, A., V. M. Kalscheuer, N. Lebrun, et al. 2014. "Expanding the Clinical Phenotype of Patients With a *ZDHHC9* Mutation." *American Journal of Medical Genetics* 164: 789–795.

Mathews, E. S., and B. Appel. 2016. "Cholesterol Biosynthesis Supports Myelin Gene Expression and Axon Ensheathment Through Modulation of P13K/Akt/mTor Signaling." *Journal of Neuroscience* 36: 7628–7639.

Mei, F., S. R. Mayoral, H. Nobuta, et al. 2016. "Identification of the Kappa-Opioid Receptor as a Therapeutic Target for Oligodendrocyte Remyelination." *Journal of Neuroscience* 36, no. 30: 7925–7935. https://doi.org/10.1523/JNEUROSCI.1493-16.2016.

Meier, F., P. E. Geyer, S. Virreira Winter, J. Cox, and M. Mann. 2018. "BoxCar Acquisition Method Enables Single-Shot Proteomics at a Depth of 10,000 Proteins in 100 Minutes." *Nature Methods* 15: 440–448.

Miles, M. R., J. Seo, M. Jiang, et al. 2021. "Global Identification of S-Palmitoylated Proteins and Detection of Palmitoylating (DHHC) Enzymes in Heart." *Journal of Molecular and Cellular Cardiology* 155: 1–9.

Mir, A., Y. Song, H. Lee, et al. 2023. "Whole Exome Sequencing Revealed Variants in Four Genes Underlying X-Linked Intellectual Disability in Four Iranian Families: Novel Deleterious Variants and Clinical Features With the Review of Literature." *BMC Medical Genomics* 16: 239.

Montag, D., K. P. Giese, U. Bartsch, et al. 1994. "Mice Deficient for the Myelin-Associated Glycoprotein Show Subtle Abnormalities in Myelin." *Neuron* 13: 229–246.

Montani, L. 2021. "Lipids in Regulating Oligodendrocyte Structure and Function." *Seminars in Cell & Developmental Biology* 112: 114–122.

Pandey, S., K. Shen, S. H. Lee, et al. 2022. "Disease-Associated Oligodendrocyte Responses Across Neurodegenerative Diseases." *Cell Reports* 40: 111189.

Quarles, R. H. 2007. "Myelin-Associated Glycoprotein (MAG): Past, Present and Beyond." *Journal of Neurochemistry* 100: 1431–1438.

Raymond, F. L., P. S. Tarpey, S. Edkins, et al. 2007. "Mutations in ZDHHC9, Which Encodes a Palmitoyltransferase of NRAS and HRAS, Cause X-Linked Mental Retardation Associated With a Marfanoid Habitus." *American Journal of Human Genetics* 80: 982–987.

Riedhammer, K. M., S. Stockler, R. Ploski, et al. 2021. "*De Novo* Stop-Loss Variants in *CLDN11* Cause Hypomyelinating Leukodystrophy." *Brain* 144: 411–419.

Rosenbluth, J., K. Nave, A. Mierzwa, and R. Schiff. 2006. "Subtle Myelin Defects in PLP-Null Mice." *Glia* 54: 172–182.

Saher, G., B. Brügger, C. Lappe-Siefke, et al. 2005. "High Cholesterol Level Is Essential for Myelin Membrane Growth." *Nature Neuroscience* 8: 468–475.

Saher, G., S. Quintes, and K.-A. Nave. 2011. "Cholesterol: A Novel Regulatory Role in Myelin Formation." *Neuroscientist* 17: 79–93.

Saher, G., and S. K. Stumpf. 2015. "Cholesterol in Myelin Biogenesis and Hypomyelinating Disorders." *Biochimica et Biophysica Acta (BBA) - Molecular and Cell Biology of Lipids* 1851: 1083–1094.

Santos, E. N., and R. D. Fields. 2021. "Regulation of Myelination by Microglia." *Science Advances* 7: eabk1131.

Schachner, M., and U. Bartsch. 2000. "Multiple Functions of the Myelin-Associated Glycoprotein MAG (Siglec-4a) in Formation and Maintenance of Myelin." *Glia* 29: 154–165.

Schirwani, S., E. Wakeling, K. Smith, DDD Study, and M. Balasubramanian. 2018. "Expanding the Molecular Basis and Phenotypic Spectrum of *ZDHHC9* -Associated X-Linked Intellectual Disability." *American Journal of Medical Genetics* 176: 1238–1244.

Schneider, A., H. Länder, G. Schulz, et al. 2005. "Palmitoylation Is a Sorting Determinant for Transport to the Myelin Membrane." *Journal of Cell Science* 118: 2415–2423.

Shimell, J. J., B. S. Shah, S. M. Cain, et al. 2019. "The X-Linked Intellectual Disability Gene Zdhhc9 Is Essential for Dendrite Outgrowth and Inhibitory Synapse Formation." *Cell Reports* 29: 2422–2437.e8.

Shin, D., S. Y. B. Howng, L. J. Ptáček, and Y.-H. Fu. 2012. "miR-32 and Its Target SLC45A3 Regulate the Lipid Metabolism of Oligodendrocytes and Myelin." *Neuroscience* 213: 29–37.

Sjöstedt, E., W. Zhong, L. Fagerberg, et al. 2020. "An Atlas of the Protein-Coding Genes in the Human, Pig, and Mouse Brain." *Science* 367: eaay5947.

Sturrock, R. R. 1980. "Myelination of the Mouse Corpus Callosum." *Neuropathology and Applied Neurobiology* 6: 415–420.

Sun, T. 2022. *Cell Type Specific Transcriptomic Characterization of Myelin Abnormalities*. Georg-August-University Göttingen. https://doi.org/10.53846/goediss-9413.

Szklarczyk, D., A. L. Gable, D. Lyon, et al. 2019. "STRING v11: Protein–Protein Association Networks With Increased Coverage, Supporting Functional Discovery in Genome-Wide Experimental Datasets." *Nucleic Acids Research* 47: D607–D613.

Thornton, M. A., G. L. Futia, M. E. Stockton, et al. 2024. "Long-Term In Vivo Three-Photon Imaging Reveals Region-Specific Differences in Healthy and Regenerative Oligodendrogenesis." *Nature Neuroscience* 27: 846–861.

Tzschach, A., U. Grasshoff, S. Beck-Woedl, et al. 2015. "Next-Generation Sequencing in X-Linked Intellectual Disability." *European Journal of Human Genetics* 23: 1513–1518.

Wang, J., J. Q. Wang, M. Y. Gao, et al. 2023. "Oligodendrocyte Lineage Cells: Advances in Development, Disease, and Heterogeneity." *Journal of Neurochemistry* 164, no. 4: 468–480. https://doi.org/10.1111/jnc.15728.

Werner, H. B., K. Kuhlmann, S. Shen, et al. 2007. "Proteolipid Protein Is Required for Transport of Sirtuin 2 Into CNS Myelin." *Journal of Neuroscience* 27: 7717–7730.

Wild, A. R., P. W. Hogg, S. Flibotte, et al. 2022. "Exploring the Expression Patterns of Palmitoylating and de-Palmitoylating Enzymes in the Mouse Brain Using the Curated RNA-Seq Database BrainPalmSeq." *eLife* 11: e75804.

Wilson, J. P., A. S. Raghavan, Y.-Y. Yang, G. Charron, and H. C. Hang. 2011. "Proteomic Analysis of Fatty-Acylated Proteins in Mammalian Cells With Chemical Reporters Reveals S-Acylation of Histone H3 Variants." *Molecular & Cellular Proteomics* 10: M110.001198.

Yamamoto, Y., R. Mizuno, T. Nishimura, et al. 1994. "Cloning and Expression of Myelin-Associated Oligodendrocytic Basic Protein. A Novel Basic Protein Constituting the Central Nervous System Myelin." *Journal of Biological Chemistry* 269: 31725–31730.

Yao, Z., C. T. J. van Velthoven, M. Kunst, et al. 2023. "A High-Resolution Transcriptomic and Spatial Atlas of Cell Types in the Whole Mouse Brain." https://doi.org/10.1101/2023.03.06.531121.

Yoshikawa, H. 2001. "Myelin-Associated Oligodendrocytic Basic Protein Modulates the Arrangement of Radial Growth of the Axon and the Radial Component of Myelin." *Medical Electron Microscopy* 34: 160–164.

Zeisel, A., H. Hochgerner, P. Lönnerberg, et al. 2018. "Molecular Architecture of the Mouse Nervous System." *Cell* 174: 999–1014.e22.

Zou, C., B. M. Ellis, R. M. Smith, B. B. Chen, Y. Zhao, and R. K. Mallampalli. 2011. "Acyl-CoA:Lysophosphatidylcholine Acyltransferase I (Lpcat1) Catalyzes Histone Protein O-Palmitoylation to Regulate mRNA Synthesis." *Journal of Biological Chemistry* 286: 28019–28025.

Supporting Information

Additional supporting information can be found online in the Supporting Information section.